Conference on Modelling Fluid Flow (CMFF'25)
The 19th International Conference on Fluid Flow Technologies
Budapest, Hungary, August 26-August 29, 2025

NUMERICAL MODEL DEVELOPMENT AND ANALYSIS OF A DROP-ON-DEMAND INKJET APPLICATION

Patrick WAGNER[1], Aurélia VALLIER[2], Hesameddin FATEHI[3]

[1] Sustainable Energy Engineering Program, Lund University, Sweden, E-mail: pa3246wa-s@student.lu.se
[2] Tetra Pak Packaging Solutions AB, Sweden, E-mail: aurelia.vallier@tetrapak.com
[3] Corresponding Author. Department of Energy Sciences, Division of Fluid Mechanics, Lund University, Lund 22100, Sweden, E-mail: hesameddin.fatehi@energy.lth.se

ABSTRACT

The print quality of drop-on-demand (DOD) systems is affected by the jet breakup and the potential occurrence of satellite droplets. This paper presents the development of a numerical model to simulate droplet formation using the volume-of-fluid (VOF) method. A particular focus is on the occurrence of satellite droplets and how different fluid properties influence jetting behavior. The research centers on a printhead with a native droplet size of 2-3 pL and limited data availability. Therefore, an inlet boundary approximation method is developed to simulate the droplet formation for different actuation waveforms accurately based on the experimental results from a JetXpert drop-watcher with two different fluids and several different actuation waveform. Results show that multi-pulse waveforms can enhance droplet detachment and mitigate satellite formation by controlling pressure dynamics in the nozzle. Further simulations on sequential multi-pulse actuation revealed residual meniscus vibrations that influence subsequent droplet formation. The model was used to investigate the effect of viscosity, density, surface tension, and contact angle on the droplet formation process.

Keywords: Drop-on-demand (DOD), Ink Jetting, Satellite Droplet, Volume-of-fluid (VOF), Newtonian Fluid, Waveform Approximation

1. INTRODUCTION

Inkjet printing is one of the most common applications of microfluidics [1]. This technology progressively creates 2D images by depositing thousands of microscopic droplets on a stationary or moving substrate. Those droplets are typically in the range of 1 to 500 pL and move at a speed of 5-8 m/s when hitting the substrate [2]. Multiple mechanisms are involved in this process and have been studied in recent years [1, 3], including the actuation method [4], the acoustics within the printhead [5], the jetting process [6] and the droplet formation and breakup [7, 8]. There are several categories of inkjet printing technologies, with the most general division between continuous inkjet (CIJ) and drop-on-demand (DOD) printers. A DOD printer uses separate pressure pulses at each nozzle to generate individual droplets that can be generated on demand. This pressure pulse and the underlying actuation mechanism strongly influence the controllability and the process of droplet formation in DOD printers.

A common actuation mechanism for DOD printers is the use of microscopic piezoelectric elements [2]. Piezoelectric elements change their shape in the presence of an electric field, which can be utilized to transfer energy to the fluid through a pressure change in the ink chamber [9]. The way these actuators produce a droplet is heavily depending on the electrical signal imposed on them. Since the piezoelectric elements are controlled with a voltage signal, two principal actuation modes can be applied. The element can either initially contract and then expand, resulting in a pull-push mode, or vice versa, leading to a push-pull actuation. Considering the delay of the electric signal and mechanical movement, this leads to a single trapezoidal pulse. This type of actuation has been subject of many numerical studies [10, 11]. Adding together multiple pulses with different amplitudes leads to the formation of more complex actuation methods and waveforms [12, 13, 5]. Apart from the electrical signal, fluid properties also influence the waveform and, consequently, jetting behaviour and droplet formation [14]. Choosing the correct waveform is essential for successfully jetting a selected ink. A simplified geometry of an inkjet nozzle is used in Figure 1 to explain the actuation process, according to [2]. A single unipolar rectangular pulse is applied to the piezoelectric element on the side of the ink chamber leading to an initial contraction. Therefore, a negative pressure pulse is induced during t_{rise}, which travels through the ink chamber

and reflects at the reservoir during t_{dwell}. When the actuator expands, the pulse is superimposed with a positive pressure pulse during t_{fall}. This positive interference leads to a high-pressure pulse that results in the droplet jetting at the meniscus.

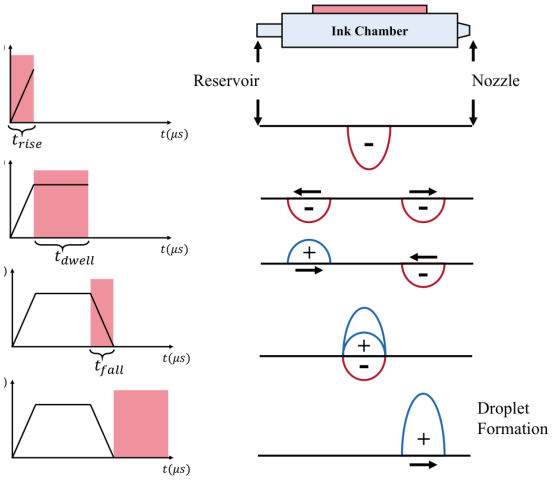

Figure 1. Schematic representation of the actuation principle, based on [2].

A comprehensive understanding of droplet formation is essential to investigate the behavior of ejected liquids. In Figure 2, the DOD droplet formation process is schematically represented and divided into six steps. Initially, the liquid is in an equilibrium state (A). After an actuation is induced, the liquid is pushed out of the nozzle (B). When a certain amount of fluid is pushed through the nozzle, the head droplet starts forming, and the necking of the fluid begins due to surface tension (C). The liquid continues to move out of the nozzle and forms an extending ligament of fluid, which attaches the head droplet to the meniscus (D). The surface tension leads to the pinch-off of the liquid ligament and the formation of a tail droplet (E). Afterwards, the liquid tail begins to catch up with the main droplet and ideally joins with it (F_a). If, however, the tail droplet pinches of from the tail and becomes an individual droplet, it is known as a satellite droplet (F_b). The head droplet formation, the pinch-off, the tail behavior, and the satellite formation are different aspects of the process that influence the final droplet size [3].

The actuation waveform is the main driver of the droplet formation and the most sensitive part of the simulation [2]. A good approximation of the inlet boundary conditions is essential to successfully simulate a DOD system. However, predicting the waveform at the boundary is challenging since the flow within the nozzle chamber is rarely observable. Some researchers have simulated the dynamics within the printhead itself, to predict the boundary condition [12, 15]. Another common method is the use of lumped element models to calculate the pressure response [11]. Analytical equations have also been used in recent papers to predict the pressure at the boundary of the numerical model [13, 5, 10]. The goal of this paper is to develop an analytical approximation method for a boundary condition for a given printhead, with limited information on its geometric characteristics, and to calibrate the boundary equation using experimental data. Through this approach, a simple model is created that can be used to investigate the effects of different waveforms on droplet formation.

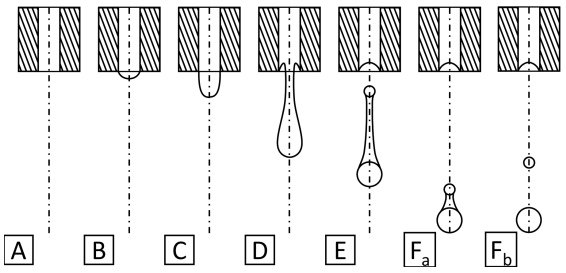

Figure 2. Six stages of the droplet formation process, based on [9]. The explanation of the different stages is presented in the text.

2. NUMERICAL MODELING

The CFD software Star-CCM+ is used for the numerical simulations in this study [16]. The VOF model was selected since it is designed to capture the interface between several immiscible fluids, since resolving the free surface is essential to capture the droplet formation process.

2.1. Volume of Fluid

The Volume of Fluid method allows the simulation of fluid dynamics of two immiscible fluids with a fluid-fluid interface (free surface). A fixed mesh is used, and the free surface moves through the mesh. At each grid cell, a volume fraction α_i is defined, indicating how much of a cell is occupied by the phase i. The material properties in a cell with $0 < \alpha_i < 1$ depend on the material properties of the constituent phases. The fluid properties in the cells are treated as a mixture. The density and viscosity are calculated as:

$$\rho = \Sigma_i \rho_i \alpha_i \tag{1}$$

$$\mu = \Sigma_i \mu_i \alpha_i \tag{2}$$

The distribution of phase i is driven by the phase mass conservation equation:

$$\frac{\partial}{\partial t}\int_V \alpha_i dV + \oint_A \alpha_i \mathbf{v}\cdot d\mathbf{a} = \int_V \left(S_{\alpha_i} - \frac{\alpha_i}{\rho_i}\frac{D\rho_i}{Dt}\right)dV - \int_V \frac{1}{\rho_i}\nabla\cdot(\alpha_i\rho_i\mathbf{v}_{d,i})\,dV \tag{3}$$

where $\mathbf{a}$ is the surface area vector, $\mathbf{v}$ is the mixture (mass-average) velocity, $\mathbf{v}_i$ is the mass-average phase velocity and $\mathbf{v}_{d,i} = \mathbf{v}_i - \mathbf{v}$ is diffusion velocity. S_{α_i} is a

source term of phase i, and $\frac{D\rho_i}{Dt}$ is the material derivation of the phase density ρ_i. For a two-phase flow, the equation is solved only for the primary phase, which in this case is the liquid.

To simulate two immiscible phases, a sharp interface between them is essential. Star-CCM+ uses the High-Resolution Interface Capturing (HRIC) scheme, based on the normalized variable diagram (NVD) [16]. Recent versions of the VOF model include the surface tension via the continuum surface force (CSF) approach. This approach includes surface tension effects as a source term in the Navier-Stokes equations.

The other governing equations include mass conservation and momentum equation. The total mass conservation for all phases is given by:

$$\frac{\partial}{\partial t}\left(\int_V \rho dV\right) + \oint_A \rho \mathbf{v} \cdot d\mathbf{a} = \int_V S\, dV \tag{4}$$

where S is the mass source term, which is defined as:

$$S = \sum_i S_{\alpha_i} \cdot \rho_i \tag{5}$$

This total mass conservation is related to the phase mass conversion (Eq. 3) and includes the fluid mixture through the density. The momentum equation is defined as:

$$\frac{\partial}{\partial t}\left(\int_V \rho \mathbf{v} dV\right) + \oint_A \rho \mathbf{v} \otimes \mathbf{v} \cdot d\mathbf{a} = -\oint_A p\mathbf{I} \cdot d\mathbf{a} + \oint_A \mathbf{T} \cdot d\mathbf{a} + \int_V \mathbf{f}_b dV - \sum_i \int_A \alpha_i \rho_i \mathbf{v}_{d,i} \otimes \mathbf{v}_{d,i} \cdot d\mathbf{a} \tag{6}$$

where p is the pressure, I is the unity tensor, T is the stress tensor and f_b is the vector of body forces.

2.2. Computational Domain

To reduce computational cost, an axisymmetric model was chosen. The simulation domain of the stand-alone jetting model includes parts of the pressure channel, the nozzle, and an air section as presented in Figure 3. The pressure channel has a radius of r_P and a length of l_P. The nozzle is formed into the nozzle plate with a thickness of l_N and has a nozzle radius of r_N. The nozzle has an angle Φ and a neck thickness l_{neck}. The air section has a length of l_A and a radius of r_A. The dimensions of the air section must be sufficiently large to prevent any backflow and boundary condition effects affecting the droplet simulation. Moreover, the air domain should be large enough to capture the crucial aspects of droplet formation. Both the pressure channel and the nozzle are filled with liquid at the start of each simulation.

Several simulations were performed to evaluate the optimal mesh type and resolution, resulting in the selection of a polyhedral mesh. A general guideline is to aim for 10 grid cells to simulate spatial details [3] accurately. For the droplet formation, the smallest length scale is the viscous length scale L_μ, which depends on γ, the surface tension coefficient:

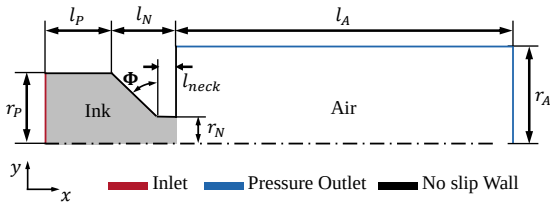

Figure 3. Schematic of the axisymmetric computational domain, including the pressure channel, nozzle, and air region.

$$L_\mu = \frac{\mu^2}{\rho\gamma} \tag{7}$$

This length scale varies depending on the properties of the liquid but is considered to be around 1-5 μm with typical values for fluid properties. This would result in a minimal element size of 0.1-0.5 μm to resolve all flow characteristics.

The minimal element size variation was chosen with the values 1.6 μm, 0.8 μm, 0.4 μm, and 0.266 μm. An example mesh with the smallest element size of 0.8 μm is shown in Figure 4. The refinement zones marked in the top half of this figure were chosen to both capture the meniscus motion within the nozzle and the droplet formation. A base element size of 5 μm was chosen in the coarse zones. A slow growth rate was selected to create a smooth transition between the refinement zone and the coarser mesh area.

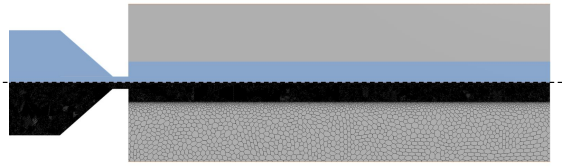

Figure 4. Unstructured mesh of the axisymmetric model. (Top) Refinement zones capturing meniscus motion and droplet formation. (Bottom) Example mesh with a smallest element size of 0.8 μm.

To investigate the mesh dependency and numerical model parameters, a simple velocity waveform, based on the simplifications presented in Figure 1, is used on the inlet. A pull time of 1 μs and a push time of 2 μs was chosen. The printhead in the simulation has a nozzle diameter of 32 μm. For the initial simulation a general time-step of 2e-7 seconds was selected with an adaptive time-step based on the CFL number of the free surface. The CFL limit was set at a maximum condition value of 0.4 and the implicit solver SIMPLE was selected. The arbitrary fluid parameters are $\rho = 1050\ kg/m^3$, $\mu = 7\ cP$, and $\gamma = 72\ mN/m$, resulting in a Ohnesorge number of 0.201. The results of the simulations are presented

in Figure 5, which shows the volume fraction of liquid within the domain. A clear difference can be observed in the tail breakup and the free surface interface between mesh (a) and the rest of the simulations. Mesh (c) and (d) show a sharp free surface interface and a similar droplet behavior.

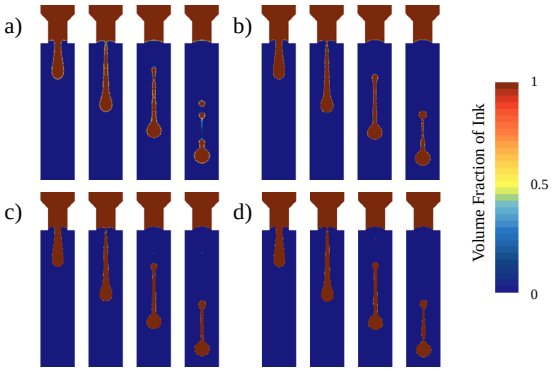

Figure 5. Simulation of the droplet formation at different mesh resolutions with an unstructured mesh at 5, 10, 15 and 20 μs, respectively. Smallest element size: a) 1.6 b) 0.8 c) 0.4 d) 0.266 μm.

When comparing the position and the velocity of the head droplet to the nozzle (Figure 6), similar results between different mesh resolutions could be observed. Both position and velocity show consistency across different resolutions. Since a mesh resolution of 0.4 μm showed a sharp free surface interface with a stable droplet formation, this mesh resolution was selected for further investigations with a total of 660514 cells.

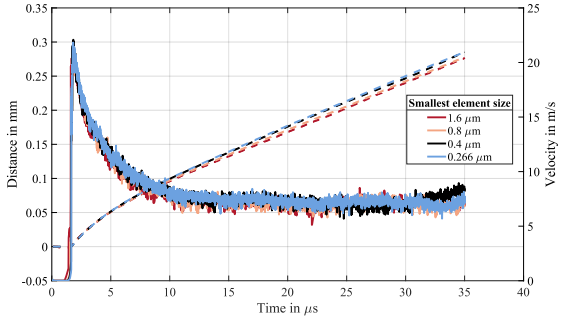

Figure 6. Distance (- -) and velocity (-) of the head droplet over time at different mesh resolutions with an unstructured mesh.

3. EXPERIMENTAL SETUP

Experimental studies were conducted to explore the formation of droplets with a specified printhead. A Newtonian fluid was selected for the experiments. This allows for an accurate description of the fluid properties without requiring complex fluid models. A mixture of 1.2 propandiol and water was chosen for this purpose. To investigate the influence of different fluid properties, two mixtures were studied. The mixtures were based on mass fractions, and the desired composition was mixed in laboratory glass vessels using a commercial scale. The two mixtures have a 1.2 propandiol content of 50% and 25%, respectively. They are referred to as mixture M_{50} and M_{25} in the following sections.

The studies were performed with a Samba printhead from Fujifilm Dimatix. This printhead produces a native droplet size of roughly 3 pL and supports fluids with a viscosity range of 4-9 cP. A single printhead holds 2048 individual nozzles each controlled by separate Silicon MEMS (microelectromechanical system) actuators. Every nozzle is connected to a common refill channel that supplies the ink chamber with a constant flow of ink and is pressurized. The ink flows through the chamber and leaves the printhead through a combined recirculation channel. A piezoelectric actuator on top of the ink chamber can induce the necessary actuation waveform to produce a droplet at the nozzle. Each nozzle has a diameter of 17 μm and is cut into a 50 μm thick nozzle plate with an angle Φ of 45 degrees.

A dropwatcher is directly connected to a JetXpert measurement software, which captures images of the droplet formation and provides multiple analysis tools. The dropwatcher of JetXpert consists of three parts: the printhead with a custom mounting plate, a high-speed LED strobe light, and the high-resolution camera system. All three components are synchronized so when the printhead fires a droplet, the strobe light flashes, and the camera records the droplet in flight at a specific delay. The resolution of the camera is half a micron, and it has an 8 million fps-equivalent exposure time. The printhead can be moved laterally to focus the camera on a single nozzle. The fluid is supplied and recirculated by a heated pipe system. The extracted data consists of image sequences from the JetXpert measurement software which have been used to calculate the velocity and position of the droplets at different timesteps. The delay between each image is 5 μs.

For the experimental investigation, five different pulse widths (t_{dwell}) with an amplitude of 18 V have been selected: 1.65, 1.97, 2.294, 2.55, 2.87 μs. Additionally, several different amplitudes at a constant pulse width of 1.97 μs were tested. Besides the single-pulse actuation, multi-pulse waveforms have been tested. Two tested multi-pulse signals are presented in Figure 11. For both multi-pulse signals, the mixture M_{50} was selected. The first waveform (a) consists of two trapezoidal pulses with the same amplitude. The second waveform (b) consists of three pulses with changing amplitudes. The first two pulses mainly increase the volume of the droplet, while the task of the final pulse is the collection of the tail. It can be observed that the produced droplet from this waveform has an even higher volume and no remaining satellite droplets in comparison to the two-pulse waveform.

4. RESULTS AND DISCUSSIONS

4.1. Calibration and Validation

The movement of the piezoelectric element generates an acoustic wave and a volumetric change that propagates through the ink chamber. This can be translated into a pressure change within the chamber, that can be used as a boundary condition for the CFD model. Since the timescale is short and the travel times are fast, it is assumed that the pressure within the chamber is approximately the same everywhere. At the beginning of an actuation signal, the system is in an equilibrium state. When the piezoelectric actuator expands due to a voltage signal, it creates a lower pressure in the ink chamber (see Figure 1). This low pressure is balanced out over time and falls back to the previous pressure level of the system. Two factors can be seen as responsible for the pressure to go back into its state of equilibrium: the retraction of the meniscus and the fluid flow through the recirculation and re-fill channel. When the piezoelectric element falls back into its non-actuated state, it creates a pressure increase in the ink chamber. This pressure increase is balanced out by the movement of the meniscus, optimally resulting in the formation of a droplet.

To translate the relation between the observable voltage input signal to the unknown pressure change within the printhead, the system is simplified to behave like a resonance circuit. This is based on the Lumped element model approach, which makes the analogy that the electric current (i) and the voltage (V) are equivalent to the volumetric flow rate (Q) and pressure difference (ΔP), respectively. In the resonance case, the system reacts to a change of state with an exponentially damped sinusoid function [17]. The function of the response can be written as:

$$V = Ae^{\zeta t} \sin\left(\frac{2\pi}{\omega}t\right) \tag{8}$$

where A represents the amplitude of the oscillation, ζ the damping factor, and ω the wave period. Applying the aforementioned analogy, the voltage represents the pressure difference and the amplitude of the oscillation depends on the amount of change from the equilibrium state. This results in the following equation:

$$\Delta P = A_p e^{\zeta t} \sin\left(\frac{2\pi}{\omega}t\right) \tag{9}$$

$$A_p = \beta A_V \tag{10}$$

where A_p is the amplitude in Pa, A_V is the amplitude in V, and β is a constant with the unit Pa/V. The voltage signal to the piezoelectric actuator leads to an expansion and contraction of the actuator. This movement leads to a decrease and increase in pressure within the ink chamber. The pressure increase is considered the same everywhere, and the actuation instantaneous. This results in two natural responses of the resonance circuit, which are induced at the beginning of each actuation, as presented in Figure 7. The pull motion of the actuator leads to a negative pulse, while the push motion results in a positive pulse.

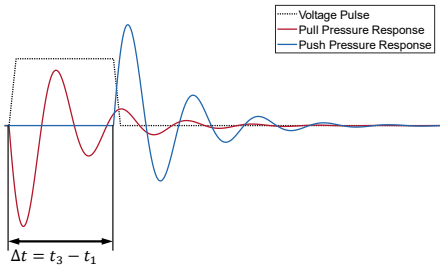

Figure 7. Schematic representation of two pressure wave responses, concerning a voltage signal.

Both responses are superimposed to create the final pressure waveform, which is used as the inlet condition for the numerical model. The amplitude of the response is directly coupled to the amplitude of the voltage signal with the constant β. The final equation for a single voltage pulse response as a pressure waveform depends on the time of the responses and the previous parameters. It can be written as:

$$\begin{aligned}
\Delta P(t) &= 0 && (t < t_1) \\
\Delta P(t) &= A_p e^{\zeta(t-t_1)} sin\left(\frac{2\pi}{\omega}(t-t_1)+\pi\right) && (t < t_3) \\
\Delta P(t) &= A_p e^{\zeta(t-t_1)} sin\left(\frac{2\pi}{\omega}(t-t_1)+\pi\right) \\
&\quad + A_p e^{\zeta(t-t_3)} sin\left(\frac{2\pi}{\omega}(t-t_3)\right) && (t >= t_3)
\end{aligned} \tag{11}$$

where t_1 is the time of the first response, and t_3 is the timing of the second response. This function can be implemented as a field function within StarCCM+ and provides a basis for data fitting with the experimental results by calibrating the parameters. The first step of the calibration process is to select a fitting wave period ω. The experimental results showed, that a sweep across multiple pulse widths results in a near quadratic relationship to the droplet velocity and position over time. This effect is based on the superimposing waveforms of the push pulse and the residual vibration of the pull pulse. At an optimal interference, the pressure peak results in a maximum velocity of the resulting droplet. To recreate this effect, different pulse widths have been simulated, using an amplitude of $A_p = 1.6$ bar, a period of $\omega = 5.2\,\mu s$ and a dampening factor of $\zeta = 250000$. The value Δt was varied in intervals of ±10% starting from $\Delta t = \omega/2$, by changing t_3 in equation 11.

To test the connection between the resonance frequency and optimal pulse width, the same simulations have been repeated for multiple values of ω. In Figure 8, the resulting relative droplet position for

different pulse widths and values of ω are presented. It can be seen that a sweep across Δt results in the described quadratic relationship and a change in resonance period corresponds to a shift of the distribution. This supports the assumption that the optimal droplet ejection is achieved when the pulse width is aligned with the resonance period, which changes with material properties. The slopes of the different distributions are affected by the velocity of the droplet and time when the data is extracted. It is therefore important to focus on the position of the maximum.

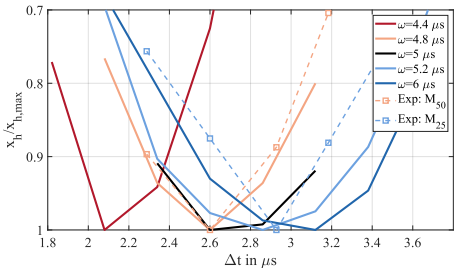

Figure 8. Simulation results of the relative droplet distance resulting from different pulse widths and resonance frequencies. All distances are derived at the same timestep of 50 μs.

To further calibrate the model, the parameter β is used to match the speed of the ejected droplet in the simulation with that in the experiment. In both cases a linear increase in the amplitude results in a linear increase of the droplet speed. The last step of the calibration consists of the definition of a dampening factor ζ. This was achieved by comparing the oscillation of the meniscus in the simulation with that in the experiments. With the designed and calibrated model, a close match between the experimental results and simulated droplet formation across multiple single pulse signals was achieved. Figure 9 shows a visual comparison between experiments and simulation for a case with an actuation amplitude of 15 V. Figure 10 shows the comparison between the recorded and simulated trajectory of multiple actuation amplitudes.

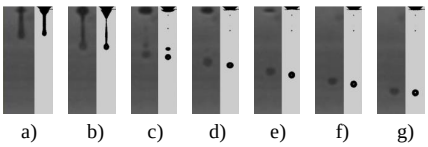

Figure 9. Comparison between experimental results (left) of a droplet formation with an actuation amplitude of 15 V and the simulation (right) with the calibrated model. The images are taken at 10, 15, .., 40 μs, respectively.

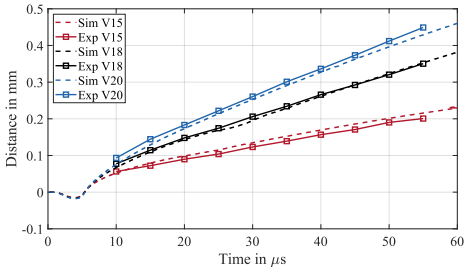

Figure 10. Trajectory comparison between experimental droplets and simulated droplets at different voltage amplitudes showing the distance (x_h) of the head droplet to the nozzle plate.

4.2. Application to different waveforms and fluids

To explore different actuation methods, the two multi-pulse waveforms are used as boundary condition with the calibrated model. For this application, the pressure waveform equation 11 was extended by two additional responses for every added voltage pulse. By superimposing all functions, a combined pressure boundary condition was approximated. The transformed waveforms for both input signals are displayed in Figure 11.

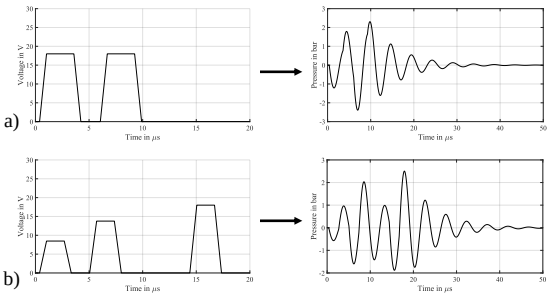

Figure 11. Computed pressure waveform for the multi-pulse actuation. (a) M-shaped waveform with two trapezoidal pulses, (b) complex waveform with three unipolar pulses.

The results of the M-shaped waveform simulation are shown in Figure 12a. A good approximation of the experimental droplet formation could be achieved. The effect of two pulses is visible in the simulation and the experimental observation. After an initial actuation, the second pulse leads to an increase in droplet volume. The final droplet in the experiments consists of a single droplet with a smaller satellite. The same result was predicted with the simulation. Nevertheless, a difference in final velocity can be observed. When comparing the simulations of the three-pulse waveform with the experimental observations, presented in Figure 12b, a close resemblance of the droplet formation was achieved. Two smaller initial pulses lead to the increase in volume,

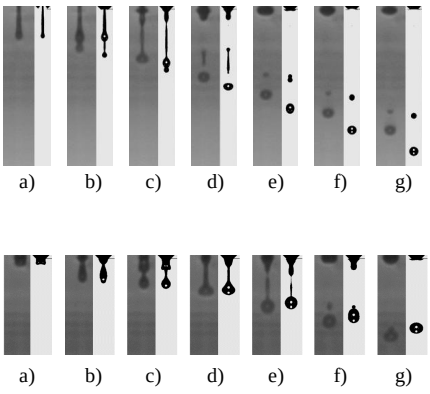

Figure 12. Comparison of experimental and simulated droplet formation using amplitude of 18 V and (a) M-shaped waveform, (b) complex waveform. The images are taken at 10, 15, .., 40 μs, respectively.

while the last pulse collects the tail and leads to a satellite-free droplet. The entire process could be recreated in the simulation. However, the final velocity still slightly differs from the observed experiments.

Besides multi-pulse actuation modes, different concentrations of 1.2 propandiol have been subjected to experimental tests. The numerical fluid parameters in the model were adjusted to examine the performance of the model when using a different fluid. Accordingly, the boundary condition approximation was adapted by selecting a different wave period ω based on Figure 8. The other boundary parameters were not varied from the previous calibration, assuming that ω mainly depends on the fluid properties, while β mainly depends on the displaced volume. The simulation of this fluid showed also a good agreement with the experimental results, as shown on Figure 13.

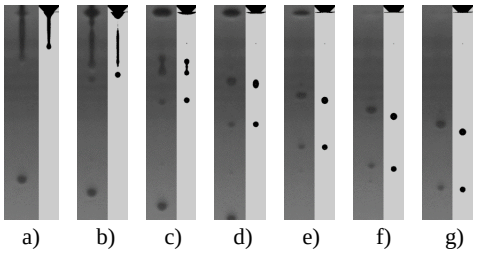

Figure 13. Comparison of experimental and simulated droplet formation for mixture M_{25} using a single trapezoidal waveform. The images are taken at 10, 15, .., 40 μs, respectively.

When simulating a multi-pulse actuation waveform, it is important to consider potential residual vibrations resulting from sequential actuation. In the observed experiments, as presented in Figure 14, it can be noted that the meniscus does not fully retract into the nozzle plate before the next droplet is fired. This can imply that the following droplets are affecting each other at the chosen frequency based on the residual vibration. For all single pulse actuation, the meniscus fully retracts before the next actuation.

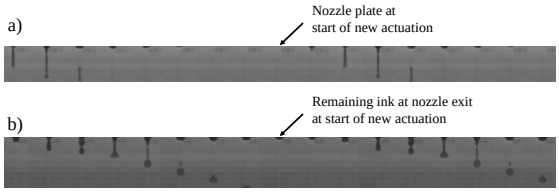

Figure 14. Experimental observations of two actuation cylces of a single pulse actuation (a) and a multi-pulse actuation (b). The arrow indicates the beginning of a new actuation cycle. Remaining ink at the nozzle can be detected during the multi-pulse actuation.

To simulate a possible case with multiple droplets, the complex waveform is repeated four times within the simulation, resulting in four individual droplets. The resulting waveform with the current model is shown in Figure 15. A clear overlapping between the separate actuation is visible. The frequency of the actuation is 20 kHz.

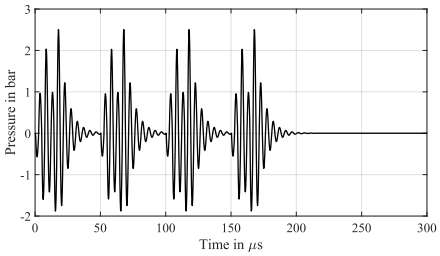

Figure 15. Pressure waveform for a multi-shot simulation with overlapping vibrations between different actuation phases.

When simulating this waveform, a different behavior between the first droplet and the following droplets can be observed, as shown in Figure 16. The first droplet moves with a significantly higher velocity, while the following droplets are slowed down. The difference in the actuation can also be seen in the meniscus movement. When simulating a single droplet, the effect of the previous droplet on the actuation waveform might not be captured. These show that while multi-pulse actuation effectively reduces satellite formation, residual meniscus vibrations in sequential jetting can alter droplet velocity and trajectory, which is of special importance for high-frequency applications.

5. PARAMETER STUDY

With the calibrated model, different fluid and printhead properties were investigated and their influence on jetting behavior with the given printhead

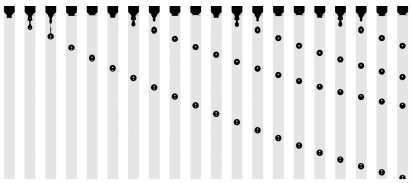

Figure 16. Sequential images of the multi-shot simulation. The images are taken at a rate of 10 μs beginning at 10 μs after the actuation.

dimensions was analyzed. This initial analysis of different fluid properties did not take into account a changing wave period and therefore only allows for a general guideline. An increase in density showed a reduction in jetting velocity and droplet volume while slightly delaying the time of pinch-off. A change in viscosity showed a strong influence on the droplet velocity and volume, as well as the pinch-off timing. Both velocity and volume greatly decreased with an increase in viscosity while the pinch-off time was delayed. An increase in surface tension showed a faster pinch-off and an increase in maximum jetting velocity while only slightly affecting the droplet volume and final velocity. For the given printhead, a change in contact angle only affected the droplet formation when reaching a non-wetting behavior. An increase in contact angle over that point resulted in a decrease in velocity and volume. The effects of viscosity are considered the most influential, given the strong fluctuation of ink viscosity depending on temperature changes.

6. CONCLUSION

A numerical stand-alone model of the jetting process from a DOD printhead was successfully developed. The model was designed to simulate an existing printhead with limited available data by incorporating a resonance circuit assumption and calibrating the boundary condition using experimental observations. A good agreement between the numerical and experimental results was achieved across multiple actuation waveforms and different fluid compositions.

The study confirmed that multi-pulse actuation improves droplet formation by controlling tail breakup and reducing satellite formation. However, new simulations demonstrated that sequential actuation leads to residual meniscus vibrations, affecting the velocity and trajectory of subsequent droplets. These results emphasize the importance of considering inter-droplet interactions in waveform optimization for high-frequency printing applications.

ACKNOWLEDGMENTS

This work was financed by Tetra Pak® Packaging Solutions AB.

REFERENCES

[1] Lohse, D., 2022, “Fundamental Fluid Dynamics Challenges in Inkjet Printing”, *Annual Review of Fluid Mechanics*, Vol. 54 (1).

[2] Hoath, S. D., 2016, *Fundamentals of Inkjet Printing: The Science of Inkjet and Droplets*, John Wiley and Sons, Incorporated, ISBN 9783527684731.

[3] Wijshoff, H., 2008, “Structure- and fluid-dynamics in piezo inkjet printheads”, Ph.D. thesis.

[4] Ezzeldin, M., Van Den Bosch, P. P. J., and Weiland, S., 2013, “Toward better printing quality for a drop-on-demand ink-jet printer: improving performance by minimizing variations in drop properties”, *IEEE Control Systems*, Vol. 33 (1), pp. 42–60.

[5] Li, D., Sun, L., Li, Z., Wu, X., Hu, G., Ma, C., Sun, Q., Liu, Y., and Zhang, Y., 2024, “Suppression of secondary droplet for high-definition drop-on-demand inkjet by actively regulating the channel acoustic waves”, *Acta Mechanica Sinica*, Vol. 40 (3).

[6] Fraters, A., Jeurissen, R., Berg, M. v. d., Reinten, H., Wijshoff, H., Lohse, D., Versluis, M., and Segers, T., 2020, “Secondary Tail Formation and Breakup in Piezoacoustic Inkjet Printing: Femtoliter Droplets Captured in Flight”, *Physical Review Applied*, Vol. 13 (2).

[7] Driessen, T., 2013, “Drop Formation from axisymmetric fluid jets”, *University of Twente*.

[8] Zhong, Y., Fang, H., Ma, Q., and Dong, X., 2018, “Analysis of droplet stability after ejection from an inkjet nozzle”, *Journal of Fluid Mechanics*, Vol. 845, pp. 378–391.

[9] Hutchings, I. M., and Martin, G. D., 2013, *Inkjet technology for digital fabrication*, Wiley Online Library.

[10] Lei, T., Han, J., and Liu, H., 2022, “Numerical Analysis and Optimal CFD Model Verification of Piezoelectric Inkjet Printhead”, *Journal of Applied Fluid Mechanics*, Vol. 15 (4).

[11] Shah, M. A., Lee, D. G., and Hur, S., 2019, “Design and Characteristic Analysis of a MEMS Piezo-Driven Recirculating Inkjet Printhead Using Lumped Element Modeling”, *Micromachines (Basel)*, Vol. 10 (11).

[12] Yang, Z., Tian, H., Wang, C., Li, X., Chen, X., Chen, X., and Shao, J., 2023, “Piezoelectric Drop-on-Demand Inkjet Printing with Ultra-High Droplet Velocity”, *Research (Wash D C)*, Vol. 6, p. 0248.

[13] Jianjun, W., Jin, H., Chuqing, X., Hongxiao, G., Chaoyu, L., Qiang, Z., Jie, Z., Pengbing, Z., Yupeng, Y., Jinzhu, Z., Wang, G., and Ruiqi, C., 2023, "Actuation waveform auto-design of drop-on-demand inkjet for ejection droplet without satellite", *Journal of Manufacturing Processes*, Vol. 102.

[14] Jiao, T., Lian, Q., Zhao, T., and Wang, H., 2021, "Influence of ink properties and voltage parameters on piezoelectric inkjet droplet formation", *Applied Physics A*, Vol. 127 (1).

[15] Wei, H., Xiao, X., Yin, Z., Yi, M., and Zou, H., 2017, "A waveform design method for high DPI piezoelectric inkjet print-head based on numerical simulation", *Microsystem Technologies*, Vol. 23 (12), pp. 5365–5373.

[16] Siemens, 2024, "StarCCM+ Documentation", URL `www.siemens.com`.

[17] Plonus, M., 2020, *Electronics and communications for scientists and engineers*, Butterworth-Heinemann.